Journal of Solid State Chemistry 181 (2008) 2031–2040

Contents lists available at ScienceDirect

Journal of Solid State Chemistry

journal homepage: www.elsevier.com/locate/jssc

Influence of iron addition on the oxygen-deficient $Sr_{0.85}Bi_{0.15}Co_{1-x}Fe_xO_{3-\delta}$ ($0.0 \leqslant x \leqslant 1.0$) perovskites

Annika K. Eriksson [a], Fredrik Lindberg [b], Gunnar Svensson [b], Peter Svedlindh [c], Paul F. Henry [d], Sten-G. Eriksson [a], Christopher S. Knee [e,*]

[a] Department of Environmental Inorganic Chemistry, Chalmers University of Technology, SE-412 96 Göteborg, Sweden
[b] Department of Structural Chemistry, Stockholm University, SE-106 91 Stockholm, Sweden
[c] Department of Engineering sciences, Uppsala University, Box 534, SE-751 21 Uppsala, Sweden
[d] Institut Laue-Langevin, BP 156, 38042 Grenoble Cedex 9, France
[e] Department of Chemistry, Gothenburg University, SE-412 96 Göteborg, Sweden

ARTICLE INFO

Article history:
Received 10 October 2007
Received in revised form
21 April 2008
Accepted 27 April 2008
Available online 8 May 2008

Keywords:
Perovskite
Oxygen vacancies
Supercell
Spin glass
Neutron diffraction

ABSTRACT

A series of oxygen-deficient $Sr_{0.85}Bi_{0.15}Co_{1-x}Fe_xO_{3-\delta}$ ($0.0 \leqslant x \leqslant 1.0$) perovskite phases were prepared using solid-state reaction. Results of neutron powder diffraction analyses show that the introduction of Fe onto the *B*-site severely effects the long range coherence of the oxygen vacancy ordered, *I*4/*mmm* supercell, observed for the $x = 0.0$ sample. For $x = 0.1$ a smaller, $a = b \approx a_p$, $c \approx 2a_p$, *P*4/*mmm* supercell gives the best agreement to the diffraction data, whilst phases in the range $0.2 \leqslant x \leqslant 0.6$ adopt disordered cubic perovskite structures. Pseudo-cubic, $a = b \approx a_p$, $c \approx a_p$, structures are found for $x \geqslant 0.8$. Evidence of weak superstructures, reflecting local oxygen ordering, is also obtained from electron diffraction. For all oxygen-annealed phases the average structure reverts to cubic $Pm\bar{3}m$. The as-prepared samples show G-type antiferromagnetic order at room temperature. The oxygen annealed $x = 0.10$, 0.25 and 1.0 samples display low-temperature spin-glass transitions.

1. Introduction

The presence of oxygen vacancies in perovskite $ABO_{3-\delta}$ crystal lattices plays a major role in both controlling the oxidation state of the *B*-site transition metal, and determining its coordination environment. For example, removal of oxygen ions from along the [100] direction creates BO_5-square pyramids or BO_4-square planes, alternatively, BO_4-tetrahedra may be obtained if oxygen ions are removed along the [110] direction. Long range ordering of these oxygen vacancies can then expand the ideal cubic perovskite unit cell, a_p, by $\sqrt{2}a_p$ or larger depending on the displacements. For perovskite-related structures containing cobalt or iron, ordering of oxygen defects yields a variety of superstructures. $Ca_2Fe_2O_5$ [1] and $Sr_2Co_2O_5$ [2] ($ABO_{2.5}$ phases) exhibit the orthorhombic brownmillerite structure, with $a \approx c \approx \sqrt{2}a_p$ and $b \approx 4a_p$. Here, the oxygen vacancies are ordered in a layered manner resulting in sheets with tetrahedral BO_4 units that alternate with octahedral ones. New phases related to the brownmillerite structure were reported in 2003 based on the $Sr_{1-x}Ln_xCoO_{3-y}$ systems [3,4], where $Ln = Y$, Ho and Dy. These materials adopt a tetragonal (*I*4/*mmm*) supercell structure with $a \approx 2a_p$ and $c \approx 4a_p$, that consists of alternating layers of oxygen replete CoO_6 octahedra and oxygen-deficient CoO_4 tetrahedral sheets. In contrast to the chains of CoO_4 tetrahedra running along the [110] direction found for the brownmillerite structure, the tetrahedra form segregated Co_4O_{12} units. Also, as suggested by the chemical formula $Sr_{0.7}Y_{0.3}CoO_{2.62}$, additional oxygen ions are located in the tetrahedral layers so that some of the cobalt ions adopt trigonal-bipyramidal coordinations [4].

Recently, work of Lindberg et al. [5] studied the effect of replacing Co by trivalent Ga and Fe on the tetragonal supercell of $Sr_{0.75}Y_{0.25}Co_{1-x}M_xO_{2.625}$. It was found that the Fe-substituted phases contain more oxygen than the un-substituted form for $x \leqslant 0.625$, and that a disordered cubic perovskite cell is obtained at higher Fe contents, i.e. $0.75 \leqslant x \leqslant 0.875$. The un-substituted, and Ga containing ($x = 0.25$) phases, displayed ferromagnetic-like contributions to magnetisation data at 320 and 225 K, respectively, whilst this effect was suppressed for the Fe phases. Another closely related iron-containing system, $Sr_{0.8}Y_{0.2}Co_{1-x}Fe_xO_{3-y}$, was also studied by Bréard et al. [6], and here a rise in the T_c onset, a broadening of the ferromagnetic transition and negative magnetoresistance all occurred with increasing iron content.

Previous reports on perovskites with Bi^{3+} at the *A*-site include diffraction and Mössbauer studies of $Bi_{1-x}Sr_xFeO_3$ [7,8], and

* Corresponding author. Fax: +46 317722853.
E-mail address: knee@chem.gu.se (C.S. Knee).

0022-4596/$ - see front matter © 2008 Elsevier Inc. All rights reserved.
doi:10.1016/j.jssc.2008.04.037

investigations of the structure and properties of $Sr_{1-x}Bi_xCoO_{3-y}$ [9,10] that revealed formation of the *I*4/*mmm* supercell for $0.1 \leqslant x \leqslant 0.2$ [10]. Motivated by a wish to understand how the *B*-site ion controls both the crystal structure and the magnetic properties of these phases we here present an investigation of the influence of iron introduction into $Sr_{0.85}Bi_{0.15}CoO_{3-y}$ [10]. An added stimulus for the present study comes from the interest in related perovskites containing both Co and Fe, such as $Ba_{0.5}Sr_{0.5}Co_{0.8}Fe_{0.2}O_{3-\delta}$, as mixed oxide ion and electrical conductors suitable for cathode applications in solid oxide fuel cells [11,12].

2. Experimental

Samples of $Sr_{0.85}Bi_{0.15}Co_{1-x}Fe_xO_{3-\delta}$ with $(0.0 \leqslant x \leqslant 1.0)$ were prepared by mechanically grinding suitable amounts of high purity $SrCO_3$, Bi_2O_3, CoO and Fe_2O_3. This *A*-site composition was chosen as the previous study [10] revealed that the $Sr_{0.85}Bi_{0.15}CoO_{3-y}$ sample had the greatest purity. The reactants were then pressed into pellets and fired at 900 and 950 °C for similar lengths of time overnight with an intermediate regrind to obtain a homogenous phase. A final overnight firing at 975 °C was necessary for $x = 1.00$ in order to obtain a single phase. The samples were quenched to room temperature (RT) in air after every heat treatment. Approximately one-half of the as-prepared samples were then heated at 800 °C for 15 h under a flow of oxygen to produce the oxygen-annealed samples. A 240 °C/h heating and cooling rate was employed. Initial phase characterisation was carried out using powder X-ray diffraction (PXRD) data collected on a Siemens D5000 diffractometer (Cu$K\alpha$) radiation in the 2θ range of 15–60°. Neutron powder diffraction (NPD) data were collected for the as-prepared $x = 0.10$, 0.25 and 1.0 samples and $x = 0.25$ and 1.0 O_2-annealed samples at RT using the time-of-flight POLARIS instrument at ISIS, Rutherford Appleton Laboratory, UK. Further NPD data were collected for the $x = 0.20$, 0.60, 0.80, and 1.00 as-prepared samples at $T = 10$ K and RT on the D1A diffractometer ($\lambda = 1.908$ Å) at the Institut Laue-Langevin, Grenoble, France. Further data sets were collected between 400 and 600 K for the as-prepared $x = 0.2$ and 1.0 samples, and scans were also performed for their respective oxygen-annealed counterparts at RT and 10 K. Analysis of the nuclear and, where appropriate, magnetic structures proceeded using the Rietveld refinement program GSAS [13].

Transmission electron microscopy (TEM) studies were performed on small amounts of finely ground samples dispersed using *n*-butanol onto a holey carbon film supported by a copper grid. The microscopes used were a JEOL JEM3010 UHR instrument operated at 300 kV for high-resolution (HREM) studies and a JEOL JEM2000FX instrument (200 kV) was used for electron diffraction (ED).

Magnetic measurements were performed on as-prepared and O_2-annealed $x = 0.1$, 0.25 and 1.00 samples in a Quantum Design MPMS-XL SQUID magnetometer. Magnetisation versus temperature was studied between 5 and 400 K, following two different protocols: zero-field-cooled (ZFC) and field-cooled (FC). The ZFC magnetisation was obtained by cooling the sample to 5 K in zero field, turning on a magnetic field of 50 and 20 Oe for as-prepared and O_2-annealed samples, respectively, and measuring the magnetisation as the sample warmed up. The FC magnetisation was subsequently obtained by measuring the magnetisation, in the same applied field, as the sample cooled to 5 K. AC magnetisation, $M(f) = M'(f)+iM''(f)$, versus temperature was studied between 10 and 120 K for the O_2-annealed samples. Isothermal magnetisation measurements were performed at 10, 100 and 300 K; magnetic hysteresis loops were measured in the magnetic field range ± 50 kOe. In some cases, the measurement procedure was simplified and the measurement was performed by applying a large positive magnetic field (50 kOe) and measuring the magnetisation as a function of decreasing field until the magnetisation changed sign.

To monitor the oxygen uptake of the samples, thermal analysis was performed in a simultaneous thermogravimetric (TG)–differential scanning calorimeter (DSC) NETZSCH STA 409 PC Luxx thermal analyser. The samples were placed in an alumina crucible and heated from RT to 800 °C with a heating rate of 5 °C/min, and then kept at 800 °C for 30 min. The atmospheres used were mixtures of oxygen/nitrogen and air/nitrogen with individual gas flow rates of 10 ml/min.

3. Results

3.1. Analysis of powder diffraction data

The as-prepared samples were all black homogeneous phases after the 950 °C sintering with the exception of the $x = 1.0$ phase, which required further heat treatment at 975 °C. PXRD patterns for all as-prepared and O_2-annealed samples could be indexed with a primitive cubic perovskite unit cell as shown in Fig. 1 for $x = 0.2$. The shift to higher 2θ exhibited by the peaks of the oxygen-annealed phase is consistent with the oxidation of the Co/Fe ions. Initial fitting of the POLARIS NPD patterns for the as-prepared samples was preformed using a *Pm*-3*m* structural model. This produced a satisfactory result for the $x = 0.25$ and 1.0 samples with cell parameters $a = 3.8891(4)$ and $3.9035(1)$ Å. The as-prepared samples all displayed magnetic diffraction peaks at RT and a G-type AFM model with cell parameters $a = b \approx \sqrt{2}a_p$ by $c \approx 2a_p$, was used to fit this intensity. At this stage closer inspection of the $x = 0.1$ data revealed several weak reflections not accounted for by either the *Pm*-3*m* nuclear model or the magnetic structure. Therefore, analyses using *I*4/*mmm* and *P*4/*mmm* supercell models similar to that described by Knee et al. [10] for $Bi_{0.1}Sr_{0.9}CoO_{3-y}$ were performed. This approach was complicated by the weak intensity of the supercell peaks and the overlap of certain magnetic reflections. Nonetheless, as shown in Fig. 2, a sufficient improvement in the fitting of the nuclear reflections was achieved for the $a \approx a_p$, $c \approx 2a_p$, *P*4/*mmm* model favoured by $Y_{0.05}Sr_{0.95}CoO_{3-\delta}$ [14], to conclude that this structure gave the best representation of the average vacancy ordering in

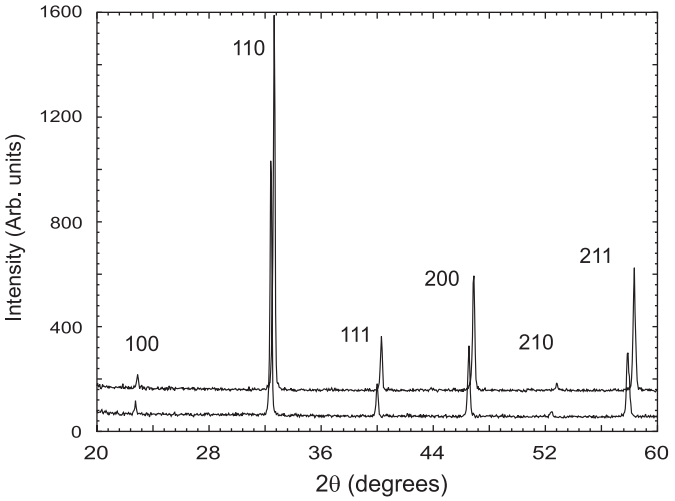

Fig. 1. PXRD patterns of as-prepared (lower) and O_2-annealed (upper) $x = 0.2$ samples. Note the shift of peaks to higher 2θ for the latter.

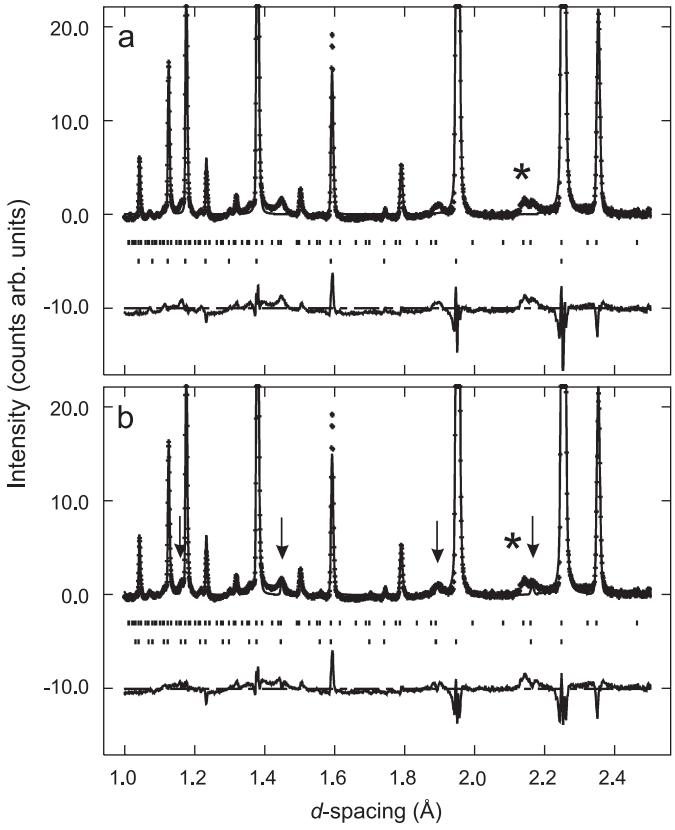

Fig. 2. Comparison of the fits achieved to the RT POLARIS data using *Pm*-3*m* (a) and *P*4/*mmm* (b) structural models for the $x = 0.1$ sample. Supercell intensity is marked by arrows and diffraction from the vanadium sample can indicated by*.

Table 1
Refined atomic and magnetic parameters for as-prepared $Sr_{0.85}Bi_{0.15}Co_{0.9}Fe_{0.1}O_{3-\delta}$ obtained from RT POLARIS data

Atom and site	*x*	*y*	*z*	$U_{iso} \times 100$ (Å^2)	Occ.
Co/Fe(1) 1*a*	0.0	0.0	0.0	1.03(7)	0.91/0.09(2)
Co/Fe(2) 1*b*	0.0	0.0	0.5	1.03(7)	0.82/0.18(2)
Sr/Bi 2*h*	0.5	0.5	0.2414(5)	1.82(5)	0.85/0.15(4)
O(1) 2*f*	0.5	0.0	0.0	5.8(3)	0.81(4)
O(2) 2*g*	0.0	0.0	0.2596(8)	2.2(2)	0.92(4)
O(3) 2*e*	0.5	0.0	0.5	2.3(2)	0.90(3)
a (Å)				3.8957(5)	
c (Å)				7.792(2)	
Vol. (Å^3)				118.25(4)	
O content				2.63(13)	
Co/Fe oxidation state				3.11(13)	
μ (μ_B)				1.24(2)	
χ^2, R_{wp}, R_p				15.25, 4.03%, 5.06%	

Space group *P*4/*mmm*.

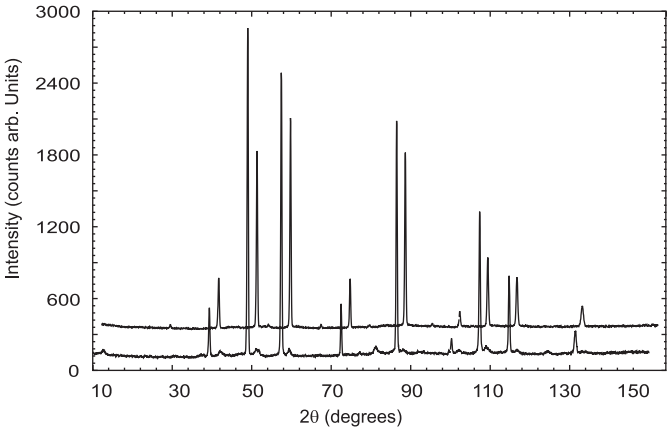

Fig. 3. Comparison of $x = 0.0$ (lower) and $x = 0.2$ (upper) as-prepared samples D1A data collected above their respective magnetic ordering temperatures. The absence of distinct supercell reflections is apparent for the $x = 0.2$ sample. Note that the $x = 0.2$ pattern is shifted horizontally and vertically to aid clarity.

the material. For the *I*4/*mmm* analysis, surplus intensity resulted on certain supercell peaks and this model was therefore discounted. The assignment of the *P*4/*mmm* structure was further supported by the reduction in χ^2 which dropped from 17 for the *Pm*-3*m* model (20 variables) to 15.3 (33 variables). The structural data derived from the *P*4/*mmm* analysis of the $x = 0.1$ sample is summarised in Table 1. From the table it can be seen that Fe showed a slight preference for the (0,0,$\frac{1}{2}$) 1*b* site, that the refined occupancies suggested a slight cobalt deficiency, and that the oxygen vacancies were distributed over the three oxygen sites. The discrepancies apparent in the close-up of the *P*4/*mmm* fit (Fig. 2b) and the fit parameters, especially χ^2, partly reflect the fact that the structural model remains an oversimplification of a more complicated oxygen ordering scheme as revealed by the electron microscopy results discussed below.

Analysis of the high-resolution, variable temperature data, collected on D1A followed a similar procedure. A comparison between the diffraction patterns of the $x = 0.0$ [10] and $x = 0.2$ samples collected at 500 and 600 K, respectively, is shown in Fig. 3. At these temperatures the patterns have no magnetic scattering present allowing assessment of the nuclear structures only. It is apparent that for the $x = 0.2$ pattern well-defined structural supercell peaks present for the $x = 0.0$ sample are absent but a modulated background indicates the existence of significant diffuse scattering. This observation was repeated for the other $x > 0.2$ samples. Closer inspection of the diffraction patterns obtained for the as-prepared series revealed an increase in the width of certain high angle reflections for samples with $x \geqslant 0.8$ as illustrated in Fig. 4. This behaviour indicated a probable lowering of unit cell symmetry for the Fe-rich samples to a pseudo-cubic, i.e. $a = b \approx a_p$, $c \approx a_p$, *P*4/*mmm* structure as found previously for $Bi_{0.1}Sr_{0.9}FeO_{3-y}$ [7]. To test this, refinements using cubic *Pm*-3*m* and pseudo-cubic *P*4/*mmm* symmetries with $a/c \approx 1$, were performed for the series. The results indicated that the cubic cell gave a good fit for $x = 0.2$–0.6 but also that the pseudo-cubic cell gave similar results concerning the *R*-values and χ^2 for this range. For the $x = 0.8$ and 1.0 samples the *P*4/*mmm* symmetry gave significantly better results which is supported by the sharp increase in the FWHM seen for $x \geqslant 0.8$ (Fig. 4b). The final Rietveld fit achieved to the 10 K data of $Bi_{0.15}Sr_{0.85}FeO_{3-\delta}$ is shown in Fig. 5. The results of the high temperature study of the $x = 0.2$ and 1.0 samples allowed antiferromagnetic ordering temperatures of ~550 and >600 K to be estimated, respectively. Details of the structural and magnetic parameters obtained from the 10 K data can be found in Table 2, and selected metal–oxygen separations for the series $x = 0.1$–1.0 are shown in Table 3. The NPD data collected for the O_2-annealed materials showed no evidence of supercell peaks from either nuclear or magnetic order. The high angle peaks also revealed no indication of broadening and all the data sets could be fitted satisfactorily using a cubic *Pm*-3*m* structural model. Full structural details for the $x = 0.2$ and 1.0 oxygen-treated samples are listed in Table 4.

3.2. Electron microscopy

Fig. 6 presents the results of a tilt series for the as-prepared $x = 0.1$ sample. These ED patterns reveal a clear doubling of one

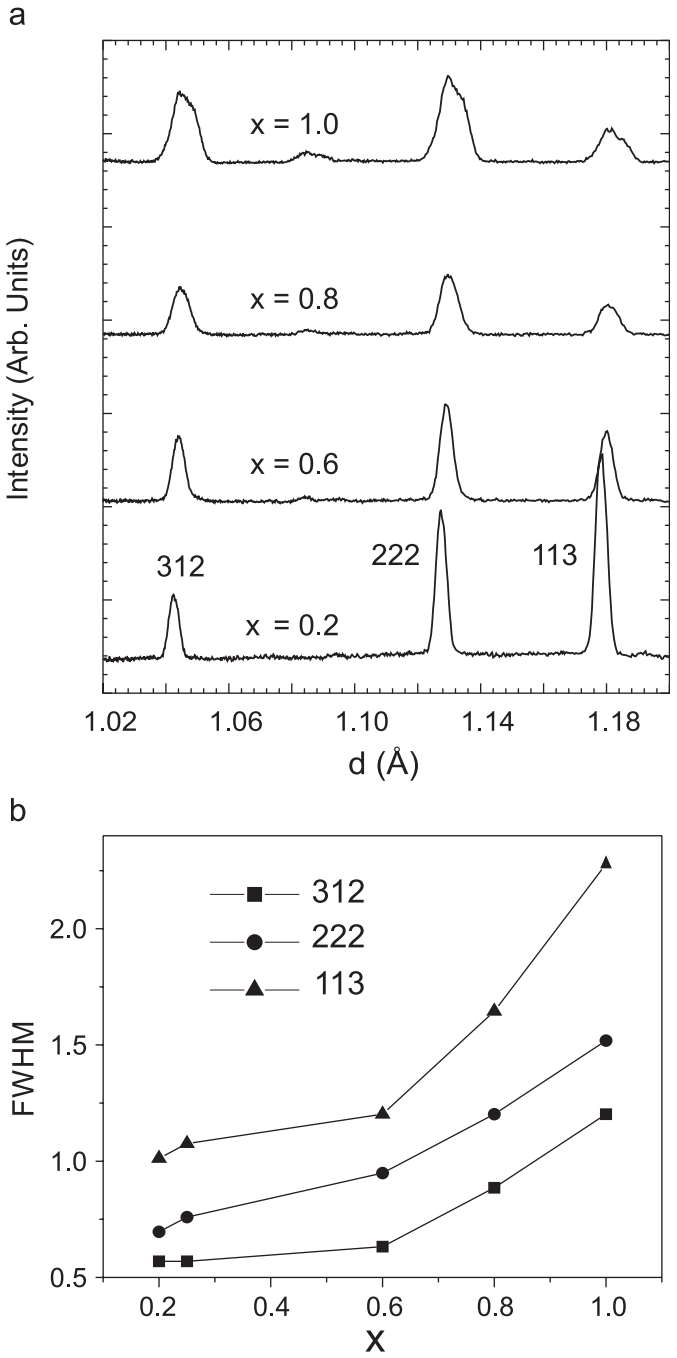

Fig. 4. Comparison of low *d*-spacing reflections (a) and FWHM (b) for as-prepared $Sr_{0.85}Bi_{0.15}Co_{1-x}Fe_xO_{3-y}$.

unit cell axes, consistent with the *P*4/*mmm* structural model employed to fit the NPD data. The $\langle 001 \rangle^*_p$ pattern reveals that this superstructure occurs in domains rotated 90° relative to each other. This is not surprising considering the very small difference in length between the perovskite sub-cell axes. (This shift of the doubling of the perovskite unit cell axis between the three different sub-cell axes was confirmed by HREM studies.) Also noteworthy are the weaker superstructure reflections in the $\langle 001 \rangle^*_p$ SAED zone axis pattern. These weak additional superstructure reflections at $\langle \frac{1}{4}, \frac{1}{2}, 0 \rangle_p$ and $\langle \frac{1}{2}, \frac{1}{2}, 0 \rangle_p$ are very similar to those reported for the $Sr_{1-x}Ln_xCoO_{2.625}$ system [15]. They can be explained by a superimposition of a tetragonal *I*-centred $a = b \approx 2a_p$, $c \approx 4a_p$ cell viewed along [100] and [001] and a

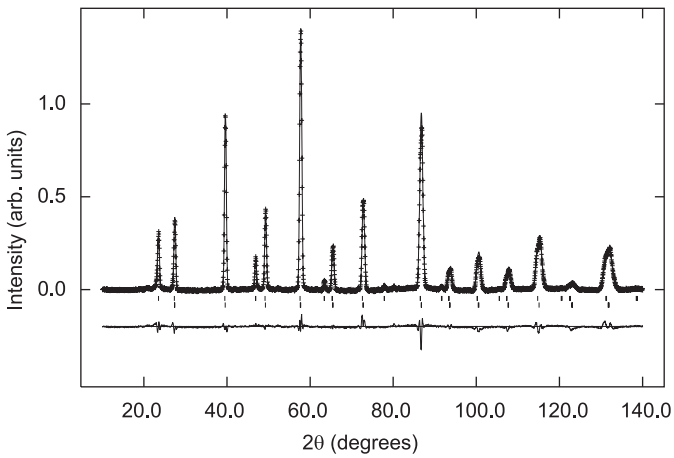

Fig. 5. Rietveld fit achieved to the 10 K D1A data for $x = 1.0$ as-prepared sample. Crosses are observed data, lines are calculated and difference plots. Lower and upper tick marks indicate reflection positions for the nuclear and magnetic structures, respectively.

brownmillerite type cell $a = b \approx \sqrt{2}a_p$, $c \approx 4a_p$ supercell viewed along [101] and [001]. These cells can also account for the superstructure reflections (arrowed) in the $\langle 102 \rangle^*_p$ SAED zone axis patterns. Similar SAED patterns was observed for the as-prepared $x = 0.25$ sample. For as-prepared $Sr_{0.85}Bi_{0.15}FeO_{3-\delta}$ ($x = 1.0$) weak superstructure reflections were seen in the SAED patterns of certain crystallites that could be indexed with $a = b = 2\sqrt{2}a_p$ by $c = 2a_p$ cell suggesting a structural similarity to $Sr_8Fe_8O_{23}$ [16].

The ED studies of the O_2-annealed $x = 0.25$ and 1.0 samples revealed that structural changes had taken place during the oxygen treatment. The SAED study of the $x = 0.25$ showed weak diffuse scattering during the first moments of exposure to the electron beam, although after a few seconds only the perovskite sub-cell reflections remained. In the O_2-annealed $x = 1.0$ sample weak superstructure reflections corresponding to a doubling of at least two perovskite sub-cell axes were apparent at the beginning of the examination (Fig. 7a) but, after prolonged exposure to the electron beam, these spots vanished leaving only the primitive perovskite sub-cell spots (Fig. 7b).

3.3. TG/DSC study

Combined TG and DSC measurements were carried out to simulate the oxygen annealing of the as-prepared samples and the results for selected samples are shown in Fig. 8. Initially, all the materials display a small mass loss attributed to evaporation of surface moisture, before at $T \sim 220$ °C a steep rise in mass occurs reaching a maximum at ~350 °C. Notably the onset of the mass increase remains fairly constant for the $0.0 \leqslant x \leqslant 0.8$ samples whilst the pure Fe phase lags approx. 40 °C behind. At $T \geqslant 350$ °C the samples start to show a decrease in mass, with many of them returning to their original mass, or lower, on reaching 800 °C. All samples showed a small increase in weight during the 30 min isotherm at 800 °C, as the oxygen content had a chance to equilibrate. One ($x = 0.2$) sample was allowed to dwell at this temperature for 12 h and revealed a total mass gain of 1.35% after cooling to RT with a 0.3% rise during the isotherm stage. Measurements in air/N_2 mixtures resulted in a shift of the onset of the mass increase to higher *T* and a reduction in the maximum amount of oxygen uptake by approx. 30%. In contrast to the other materials, the $x = 0.0$ sample showed a second increase in mass at 700 °C accompanied by a sharp exothermic event for which a

Table 2
Refined atomic and magnetic parameters for as-prepared $Sr_{0.85}Bi_{0.15}Co_{1-x}Fe_xO_{3-\delta}$, $x = 0.20$, 0.6, 0.8 and 1.0 samples from D1A data collected at 10 K

	0.2	0.6	0.8	1.0
Sr/Bi $U_{iso} \times 100$ (Å^2)	2.11(6)	1.75(6)	1.55(5)	1.63(5)
Occ.	0.85/0.15	0.85/0.15	0.85/0.15	0.85/0.15
Co/Fe(1) $U_{iso} \times 100$ (Å^2)	1.36(2)	1.10(6)	0.83(4)	1.06(5)
Occ.	0.78(1)/0.22(1)	0.37(1)/0.63(1)	0.20(1)/0.80(1)	0/1.0
O(1) $U_{iso} \times 100$ (Å^2)	3.46(6)	3.00(6)	2.76(6)	2.93(6)
Occ.	0.88(1)	0.89(1)	0.96(1)	0.98(2)
O(2) $U_{iso} \times 100$ (Å^2)	–	–	2.76(6)	2.93(6)
Occ.	–	–	0.71(2)	0.72(2)
a (Å)	3.888(1)	3.894(1)	3.895(2)	3.897(3)
c (Å)	–	–	3.902(1)	3.904(1)
Vol. (Å^3)	58.813(2)	59.058(2)	59.189(7)	59.323(9)
μ (μ_B)	2.62(2)	2.65(2)	2.50(2)	2.53(2)
O content	2.64(3)	2.67(3)	2.63(3)	2.68(4)
Co/Fe oxidation state	3.13(3)	3.19(3)	3.11(3)	3.21(4)
χ^2	3.923	4.596	3.239	4.641
R_{wp} (%)	5.46	6.81	6.05	6.94
R_p (%)	4.15	5.19	4.68	5.33

Space group for $x = 0.2$ and 0.6 is *Pm*-3*m*, Sr/Bi at (0.5,0.5,0.5) 1*b*, Co/Fe at (0,0,0) 1*a*, O(1) at (0.5,0,0) 3*d*. Space group for $x = 0.8$ and 1.0 is *P*4/*mmm*, Sr/Bi at (0.5,0.5,0.5) 1*d*, Co/Fe at (0,0,0) 1*a*, O(1) at (0.5,0,0) 2*f* and O(2) at (0,0,0.5) 1*b*.

Table 3
Selected refined interatomic distances for as-prepared samples obtained from RT ($x = 0.1$) and 10 K ($x = 0.2$–1.0) neutron diffraction data

	0.1	0.2	0.6	0.8	1.0
Sr/Bi–O(1)	2.708(3) × 4	2.750(1) × 12	2.753(1) × 12	2.756(1) × 8	2.759(1) × 8
Sr/Bi–O(2)	2.7583(4) × 4	–	–	2.754(1) × 4	2.756(1) × 4
Sr/Bi–O(3)	2.803(3) × 4	–	–	–	–
Co(1)/Fe(1)–O(1)	1.9478(3) × 4	1.944(1) × 6	1.947(1) × 6	1.947(1) × 4	1.949(1) × 4
Co(1)/Fe(1)–O(2)	2.2023(7) × 2	–	–	1.951(1) × 2	1.952(1) × 2
Co(2)/Fe(2)–O(2)	1.873(7) × 2	–	–	–	–
Co(2)/Fe(2)–O(3)	1.9478(3) × 4	–	–	–	–

Table 4
Structural parameters and refined bond distances obtained for O_2-annealed $x = 0.2$ and 1.0 samples at 10 K

Sample		0.2	1.0
Sr/Bi	U_{iso} (Å^2)	1.49(5)	1.19(4)
	Occ.	0.85/0.15	0.85/0.15
Co/Fe	U_{iso} (Å^2)	0.7(1)	0.48(4)
	Occ.	0.79 (1)/0.21(1)	1.0
O(1)	U_{iso} (Å^2)	1.91(4)	1.76(5)
	Occ.	0.94(1)	0.95(1)
a (Å)		3.8577(1)	3.8742(1)
Vol. (Å^3)		57.403(3)	58.150(3)
O content		2.82(2)	2.86(2)
Co/Fe oxidation state		3.496(4)	3.570(4)
χ^2, R_{wp}, R_p (%)		2.506, 6.52, 4.95	6.793, 7.98, 6.06
Sr/Bi–O(1) × 12		2.728(1)	2.739(1)
Co/Fe–O(1) × 6		1.929(1)	1.937(1)

Space group is *Pm*-3*m*, Sr/Bi at (0.5,0.5,0.5) 1*b*, Co/Fe at (0,0,0) 1*a*, O(1) at (0.5,0,0) 3*d*.

corresponding endotherm was not observed on cooling. Similar behaviour has previously been observed for the $Sr_{1-x}Bi_xCoO_{3-y}$, $x = 0.1$ and 0.2 samples and attributed to an irreversible structural change from the *I*4/*mmm* supercell to the cubic *Pm*-3*m* structure [10].

3.4. Magnetic properties

As expected for antiferromagnetically ordered systems below their $T_{Néel}$ the temperature dependence of the magnetisation for the $x = 0.1$, 0.25 and 1.0 as-prepared samples is basically temperature independent and the data is not shown here. In contrast the M vs. T data obtained for their oxygen-annealed counterparts (Fig. 9) reveal a strong temperature dependence with distinct cusps at $T \approx 80$ K for the $x = 0.1$ and 0.25 samples at which point the ZFC and FC measurements diverge. The behaviour of the $x = 1.0$ sample, also shown in Fig. 9, is somewhat different. Here, a temperature-independent background is observed and the temperature dependence of the magnetisation is less pronounced. Still, the ZFC and FC curves are seen to diverge at $T \approx 70$ K. The temperature-dependence behaviour suggests spin-glass-like character and this was confirmed by AC magnetisation measurements that reveal frequency-dependent freezing temperatures as shown in Fig. 10 for the $x = 0.1$ and 1.0 samples; the behaviour of the $x = 0.25$ sample is similar to that of the $x = 0.1$ sample and therefore not shown here. The AC magnetisation results obtained for the $x = 0.1$ and 0.25 samples resemble results obtained for archetypal spin-glass materials [17], while the spin-glass behaviour of the $x = 1.0$ sample "sits" on a seemingly temperature-independent background, either originating from a more complex magnetic behaviour with phase-separated spin-glass and antiferromagnetic phases or a small amount of ferro- or ferrimagnetic impurity phase.

Magnetisation vs. applied field data is shown for the as-prepared and O_2-annealed $x = 0.1$, 0.25 and 1.0 samples in Figs. 11 and 12, respectively. Here, for the as-prepared samples, there is indication of a weak ferromagnetic state as is seen from the magnetic hysteresis observed for small magnetic fields, but the dominating behaviour is the AFM order, seen in the NPD measurements, giving rise to the linearity of the magnetisation vs. field curves observed for larger magnetic fields. For the O_2-annealed $x = 0.1$ and 0.25 samples a clear hysteresis loop is apparent for the 10 K data with magnetic irreversibility extending to fields larger than 50 kOe. The origin of this unusual behaviour is

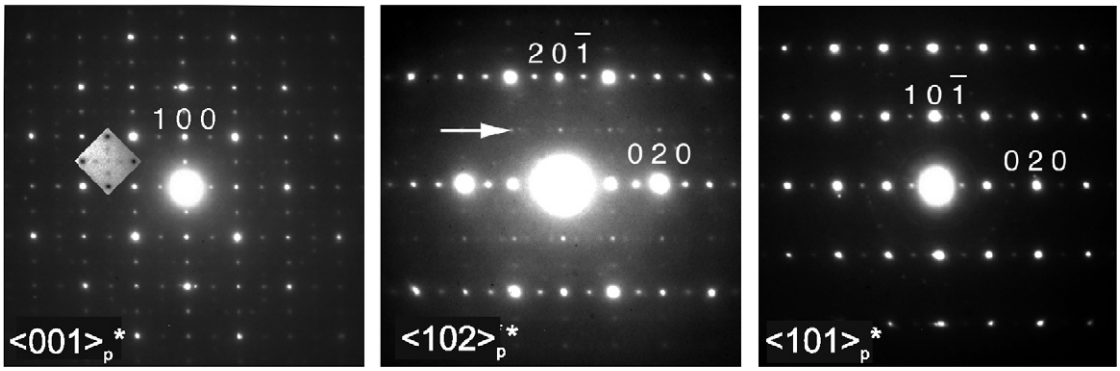

Fig. 6. SAED patterns of a crystallite found in the $x = 0.1$ as-prepared sample. In all SAED patterns strong superstructure reflections corresponding to a doubling of the perovskite sub-cell, e.g. $a = b \approx a_p$, $c = 2a_p$. The $\langle 001 \rangle^*_p$ pattern reveals that this superstructure occurs in domains rotated 90° relative to each other. In the $\langle 001 \rangle^*_p$ SAED pattern weak additional super structure reflections at $\langle 1/4, 1/2, 0 \rangle_p$ and $\langle 1/2, 1/2, 0 \rangle_p$ can be seen. The origin of these reflections is discussed in the text.

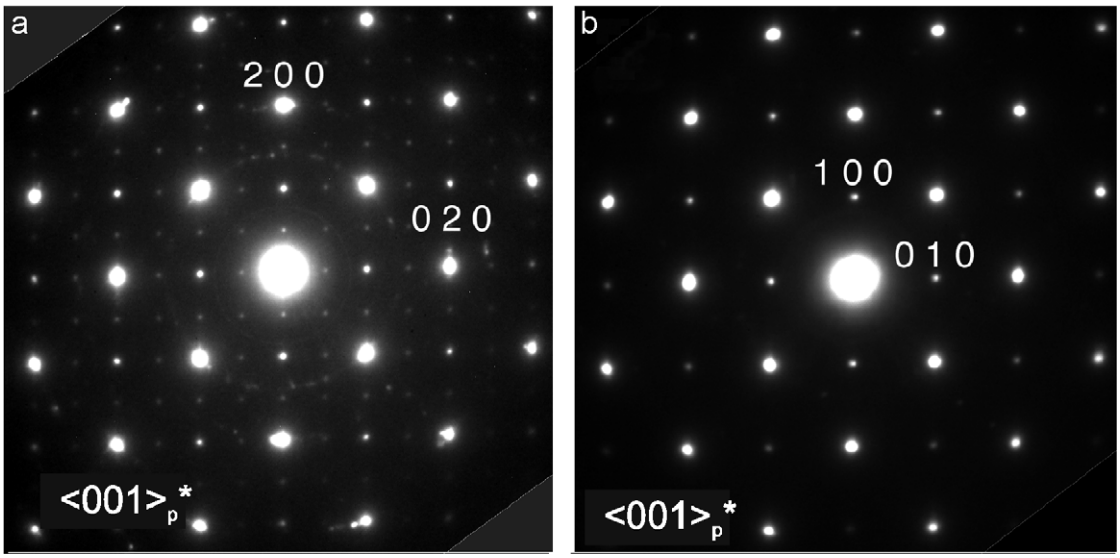

Fig. 7. SAED patterns of a crystallite found in the $x = 1.0$, O_2-annealed sample. In the pattern (a) weak superstructure reflections can be seen. These can be indexed by $a = b \approx 2a_p$ supercell. These reflections vanish upon longer exposure to the beam (b).

not fully understood, but it can be concluded that the observed magnetic hysteresis is linked to the low-temperature spin-glass phase, since the magnetic irreversibility disappears (cf. inset in Fig. 12) as the temperature is increased above the spin-glass ordering temperature. The magnetic hysteresis is much less pronounced for the $x = 1.0$ annealed sample. Comparing the magnitude of the field-induced magnetisation for as-prepared and O_2-annealed samples it is seen that it has increased substantially for the $x = 0.1$ and 0.25 samples, while the magnitude of the $x = 1.0$ sample is similar to its as-prepared counterpart. The large increase in field-induced magnetisation for the $x = 0.1$ and 0.25 annealed samples is explained by the introduction of ferromagnetic interactions, something which will be discussed further below.

4. Discussion

Based on NPD studies the crystal structures of the as-prepared $Sr_{0.85}Bi_{0.15}Co_{1-x}Fe_xO_{3-\delta}$ series evolve from an $I4/mmm$ supercell for $x = 0.0$ [10], via a $P4/mmm$ supercell for $x = 0.1$, to disordered cubic structures ($Pm\text{-}3m$) for $0.2 \leqslant x \leqslant 0.6$, before pseudo-cubic ($P4/mmm$) phases are obtained for $x \geqslant 0.8$. For the $x = 0.0$ and 0.1 samples, the long range correlation of the BO_6 and BO_{6-x} units along the c-axis requires a quadrupling and doubling of the c-parameter, respectively. The supercells, however, remain very close to integer multiples of the basic perovskite cell and the diffraction patterns of the samples appear metrically cubic. As cobalt is replaced by higher levels of iron a disordered cubic structure with a growing tetragonal character emerges. This lowering of symmetry reflects an asymmetric distribution of oxygen vacancies in the ac-plane, e.g., for $Sr_{0.85}Bi_{0.15}FeO_{3-\delta}$ the NPD refinement reveals that the occupancy of the $O(2)$, $(0,0,\frac{1}{2})$ site favours a decrease to ≈ 0.72, whilst the $O(1)$ site remains close to full occupancy (Table 2). The preferential vacancy site leads to an elongation of the cell in the c-direction rather than the contraction that may have been expected. From Fig. 13, which plots the cell parameters of the $x = 0.2$–1.0 sample, it is apparent that the average perovskite repeat unit displays a small rise with increasing Fe content, a trend consistent with the larger size of the Fe^{3+} ion. The oxidation of the B-site ions after oxygen annealing is reflected in the smaller cell parameters obtained (see Tables 2 and 4). For example the $x = 0.2$ O_2-annealed sample reveals a 0.8% contraction of the a-parameter based on the 10 K analyses. For the $x = 0.8$ and 1.0 samples oxygen treatment not only fills some of the oxygen vacancies but also removes the asymmetric distribution of vacancy sites to yield a cubic lattice.

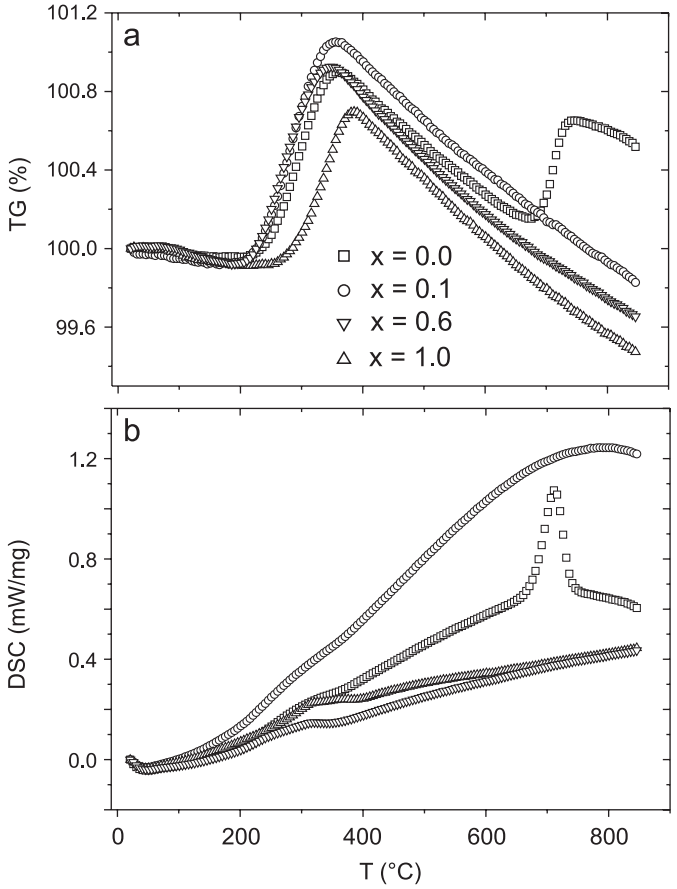

Fig. 8. TG (a) and DSC (b) results for as-prepared $x = 0.0$, 0.1, 0.6 and 1.0 samples obtained under a flow of O_2/N_2 gas mixture.

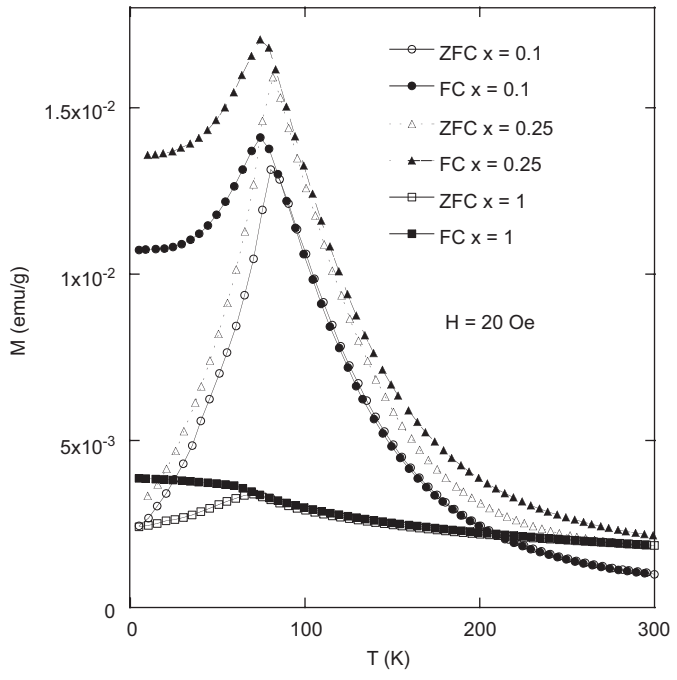

Fig. 9. Temperature dependence of M for O_2-annealed $x = 0.1$ (a) and $x = 0.25$ (b) and $x = 1.0$ (c).

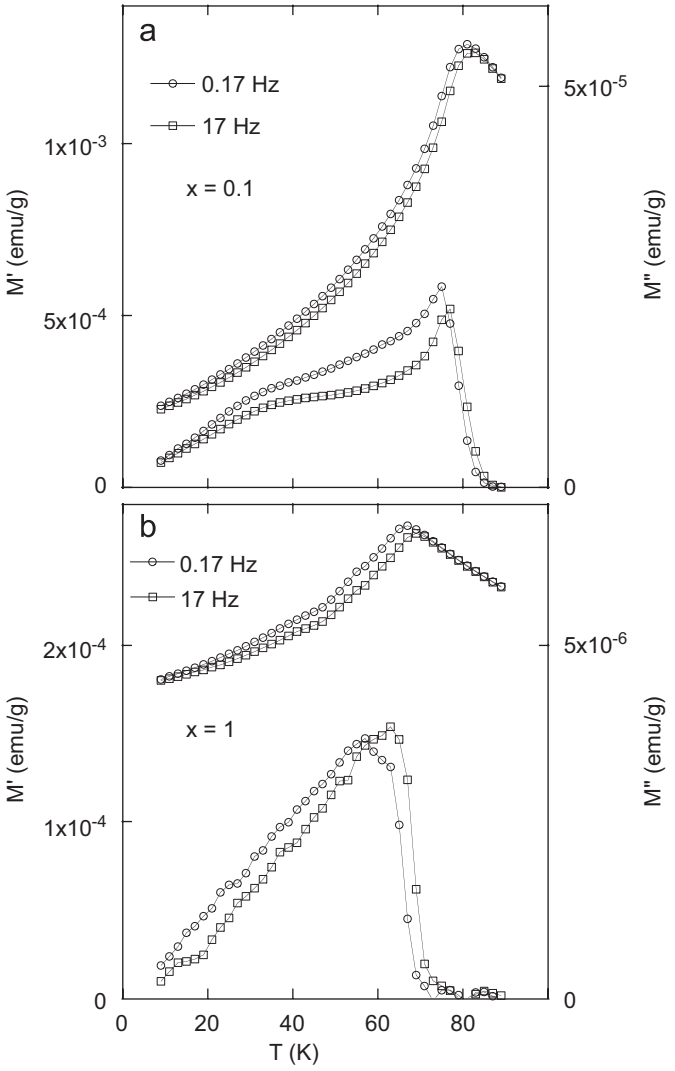

Fig. 10. Frequency dependence of the real M' and imaginary M'' components of the ac magnetisation of the $x = 0.1$ (a) and $x = 1.0$ (b) O_2-annealed sample.

The coherence of the long range oxygen vacancy ordering of the $Sr_{0.85}Bi_{0.15}Co_{1-x}Fe_xO_{3-\delta}$ series is clearly severely affected by the presence of Fe. There may be two related factors at work, either the introduction of Fe significantly increases the overall oxygen content and thus reduces the number of oxygen defects; or, alternatively, the addition of Fe produces a more disordered situation and the two distinct Co sites present in the layered *I*4/*mmm* superstructure are effectively merged into one average position with a randomized mixture of $BO_4/BO_5/BO_6$ coordinations. The refined oxygen contents of the as-prepared samples (Table 2) do not display a particularly strong dependence as a function of Fe addition, suggesting that it is the latter factor which is dominant here. It is apparent that the structural effects of Fe substitution are more dramatic for the present compounds when compared with the behaviour of the $Sr_{0.75}Y_{0.25}Co_{1-x}Fe_xO_{2.62}$ series, for which the *I*4/*mmm* supercell persists for $x \leqslant 0.625$ [5]. We suggest that the reason for this difference in the robustness of the supercells (at least on the length scale probed by NPD) is linked to the degree of *A*-site ordering in the materials. Analysis of synchrotron X-ray diffraction data for the $Sr_{1-x}Bi_xCoO_{3-\delta}$ phases has revealed the absence of Bi/Sr ordering that probably reflects the closeness in size of the Bi^{3+} and Sr^{2+} ions [18]. In contrast, for the $Ln_{1-x}Sr_x$ systems, the smaller Ln^{3+} ions (Y, Ho, Dy) strongly favour the nine-fold coordinated (0,0, $z \approx 0.35$) site associated with

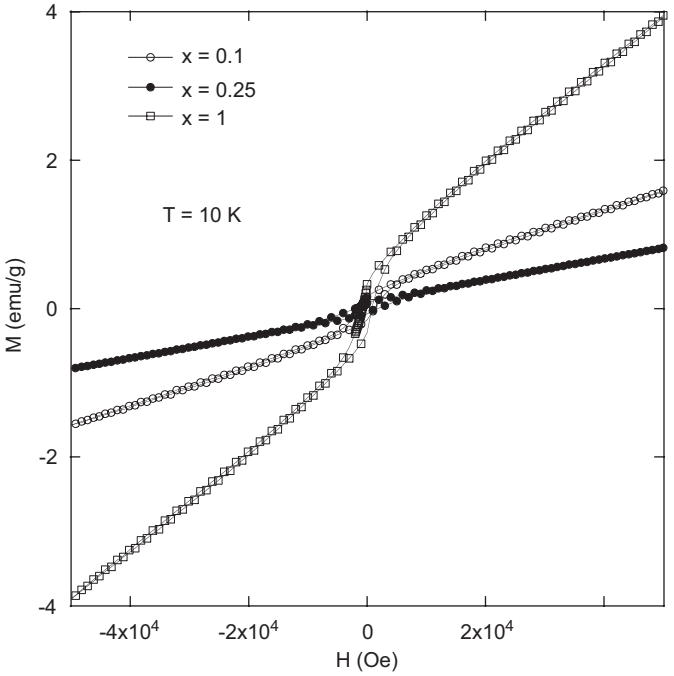

Fig. 11. Magnetisation loops at 10 K for $x = 0.1$, 0.25 and 1.0 as-prepared samples.

the oxygen-deficient BO_{6-x} layer and this provides an incentive for supercell formation regardless of the *B*-site ion.

The results of the ED/TEM studies provide further insight into the local structure of the materials and suggest that deviations from the average picture obtained from the neutron diffraction results are relatively common. Here, with care, supercell reflections are apparent for crystallites across the entire series of as-prepared samples although these do become significantly weaker with increasing levels of Fe. Oxygen annealing is also seen to have an adverse effect on the coherence of the superstructures in the materials. The sensitivity of the superstructures of these compounds to oxygen annealing, and their instability to the electron beam for the O_2-annealed samples, strongly indicates that they originate from vacancy ordering in the oxygen lattice. The delicate nature of supercell formation for these *B*-site substituted cobalt perovskites is further emphasised by the findings of Bréard et al. for the $Sr_{0.8}Y_{0.2}Co_{1-x}Fe_xO_{3-\delta}$ series. Paradoxically, no superstructure is apparent from ED results for their $Sr_{0.8}Y_{0.2}Co_{0.5}Fe_{0.5}O_{2.67}$ as-prepared sample but, after treatment under high pressure oxygen, the oxidised phase reveals a modulated structure with extra diffraction spots [6].

The estimated oxidation states of the *B*-site ions for the as-prepared samples, based on the NPD refinements, lie in the range +3.1–3.2 indicating that the majority of Co/Fe ions are trivalent (Table 2). The dynamic TG measurements (Fig. 8a) reveal that there exists an equilibrium between the oxidation of M^{3+} to M^{4+} species that occurs between approximately 250 and 350 °C and their reduction back to M^{3+} on heating above 400 °C. In fact, at $T > 700$ °C, the mass of all the samples falls below their initial mass indicating the likely presence of Co^{2+}/Fe^{2+} ions. This redox behaviour is comparable with recent findings for related $(Ba_{0.5}Sr_{0.5})_{1-x}Sm_xCo_{0.8}Fe_{0.2}O_{3-\delta}$ phases [12]. A total mass gain of 1.35% was obtained for the $x = 0.2$ sample subjected to a 12 h isotherm at 800 °C in flowing oxygen, which is in good agreement with the refined oxygen contents determined from the NPD analyses (Tables 2 and 3) that indicate a mass gain of 1.47% for the $x = 0.2$ O_2-annealed sample. After oxygen annealing the average metal valence state increases to ~+3.5 for the $x = 0.2$ and 1.0 samples; nonetheless the O_2-annealed phases remain oxygen deficient (Table 3). Theoretically a metal valence state of +3.85 is obtainable for an oxygen replete sample.

The magnetic properties of the as-prepared and O_2-annealed samples reveal significant differences reflecting the oxidation of the metal ions, and the change in the local defect structure that accompanies the oxygen treatment. The behaviour of the $x = 0.1$ and 0.25 samples is very similar to that of $Sr_{0.85}Bi_{0.15}CoO_{3-y}$ [10], with the transformation of a long range ordered antiferromagnetic state to a spin-glass phase evidenced by both the magnetisation data and the disappearance of magnetic reflections in the NPD data. The increased average metal oxidation state introduces more ferromagnetic interactions that compete with the underlying M^{3+}–O–M^{3+} antiferromagnetic coupling to produce a disordered glassy spin state. The Goodenenough–Kanamori rules [19,20] for superexchange interaction state that the interaction is strongly antiferromagnetic in case of partly occupied (or unoccupied) orbitals at two magnetic ions, while the interaction is weakly ferromagnetic in case of interaction between partly occupied and unoccupied orbitals. This implies that cations of the same kind will exhibit antiferromagnetic interaction, with the exception of d^4 cations such as Fe^{4+}, in which case the sign of the interaction depends on the direction of the superexchange, i.e., both ferro- and antiferromagnetic interaction can be expected in case of Fe^{4+}–O–Fe^{4+} superexchange. The low-temperature spin-glass state observed for the O_2-annealed $x = 0.1$ and 0.25 samples thus suggests significant contribution from ferromagnetic interactions of type Fe^{3+}–O–Fe^{4+}, Fe^{3+}–O–Co^{4+} and Co^{3+}–O–Co^{4+}. A comparison with Fig. 11 of Ref. [10] indicates that in contrast to the behaviour of the $Sr_{0.8}Y_{0.2}Co_{1-x}Fe_xO_{3-\delta}$ system the cusp observed for the O_2-annealed sample does not broaden noticeably with the addition of 25% Fe. The magnetisation data for the $x = 1.0$ phases also reveals a similar transformation from antiferromagnet to spin-glass phase, although less prominent and the magnitude of the field-induced magnetisation is reduced for this O_2 annealed system compared with the annealed cobalt-containing phases. The reason why the spin-glass behaviour is less pronounced for the $x = 1$ annealed sample could be that for this sample the oxidation state is, compared to the two other annealed samples, closer to +4. The magnetic interaction may therefore be dominated by Fe^{4+}–O–Fe^{4+} superexchange, yielding a more ordered arrangement of antiferro- and ferromagnetic interactions and thus a lesser degree of spin frustration. However, one should keep in mind that some bond disorder must exist in the annealed $x = 1$ sample to explain the absence (presence) of an antiferromagnetic (a spin-glass) phase.

Finally, we consider the ordered moments obtained from the 10 K NPD refinements for $x = 0.2$–1.0 (Table 2). Apart from an initial increase for the $x = 0.2$ sample, i.e., $\mu_{AFM} = 2.32(2)\,\mu_B$ for $Sr_{0.85}Bi_{0.15}CoO_{3-\delta}$ [10], the moments do not display any great dependence on the level of Fe substitution and lie close to $2.5\,\mu_B$ for $x = 0.2$–1.0. The magnitude of the moments is significantly lower than the values expected for HS Co^{3+} ($4\,\mu_B$) and Fe^{3+} ($5\,\mu_B$) and the anticipated increase with increasing HS Fe^{3+} content is not observed. This possibly points towards increased Fe^{4+} (HS, $S = 2$, or LS, $S = 1$) for samples with higher *x*, although there is no large increase in the refined oxygen contents of the phases across the series to support this. Moreover, magnetic moments as low as $2.5\,\mu_B$ indicate that the Hund's coupling is not the most decisive factor for deciding the occupation of the different crystal field split 3*d* orbital levels. Alternatively, the interplay of factors such as the local defect structure of the phases and the covalency of the Co/Fe–O bonds may combine to produce the observed trend of low and largely invariant moments.

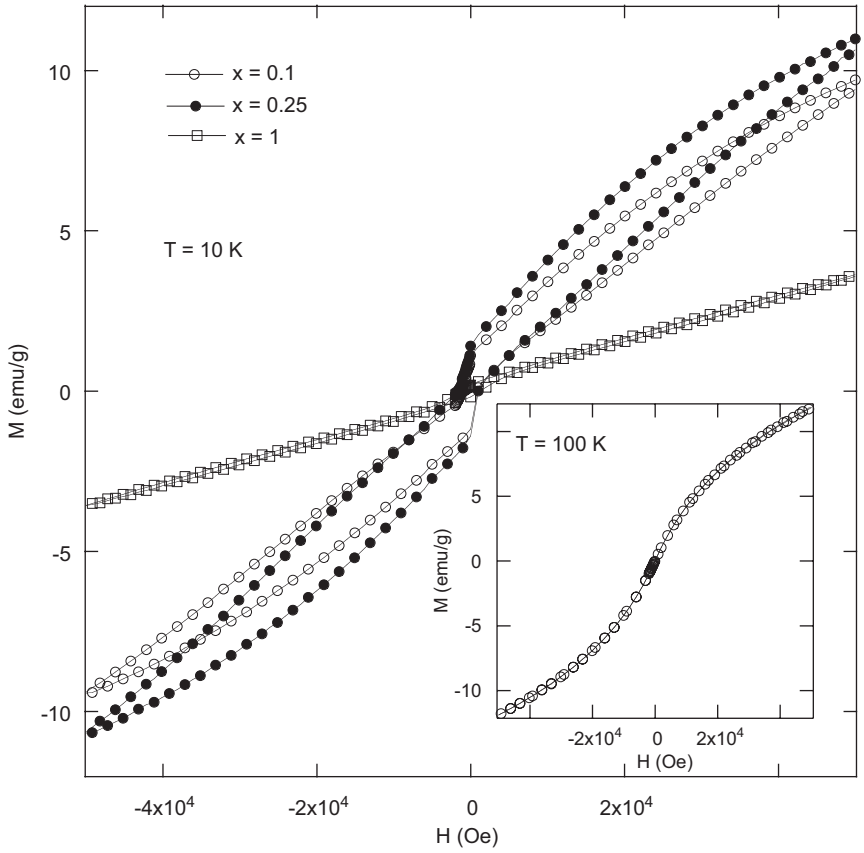

Fig. 12. Magnetisation loops at 10 K for $x = 0.1$, 0.25 and 1.0 O_2-annealed sample. Inset shows data for $x = 0.1$ collected at 100 K.

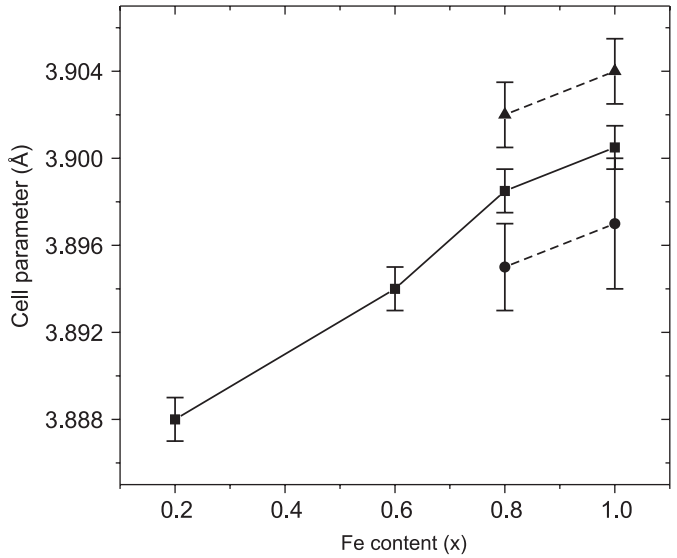

Fig. 13. Cell parameter trend for as-prepared $Sr_{0.85}Bi_{0.15}Co_{1-x}Fe_xO_{3-\delta}$ obtained from 10 K data. For the tetragonal $x = 0.8$ and 1.0 samples, the mean repeat perovskite sub-cell (a_p) is also shown.

5. Conclusion

In summary an investigation of the effect of iron substitution for cobalt on the structure and magnetism of the $Sr_{0.85}Bi_{0.15}Co_{1-x}Fe_xO_{3-\delta}$ perovskites has revealed an evolving picture of supercells and disordered structures that reflects the coherence of oxygen vacancy order. The long range coherence of the supercells for these bismuth-stabilised perovskite phases proves to be far more sensitive to iron addition than their lanthanide analogues. Oxygen annealing simplifies all the structures to cubic although even here evidence of cell doubling persisting on an extremely short range scale is seen in the ED pattern of $Sr_{0.85}Bi_{0.15}FeO_{3-\delta}$ The increased oxygen content also destroys the long range antiferromagnetic order of the magnetic moments for all samples. Further studies into the redox properties and electrical conductivity of these phases are currently in progress.

Acknowledgments

We thank the Institut Laue-Langevin and the ISIS facility for the provision of neutron diffraction beam time and Ron Smith (POLARIS, ISIS) for technical assistance during the experiments. Stefan Norberg is also thanked for data collection at ISIS. This research project has been partly funded from the Swedish research council and the Foundation for Strategic Research (Complex Oxide and FRAM programmes). P.S. acknowledges the Knut and Alice Wallenberg Foundation (KAW) for funding in support of the QD MPMS system. The data collection at ISIS was supported by the European Commission under the 6th Framework Programme through the Key Action: Strengthening the European Research Area, Research Infrastructures. Contract no. HII3-CT-2003-505925.

References

[1] A.A. Colville, Acta Crystallogr. B 26 (1970) 1469.
[2] J.C. Grenier, S. Ghodbane, G. Demazeau, M. Pouchard, P. Hagenmuller, Mater. Res. Bull. 14 (1979) 831.
[3] R.L. Withers, M. James, D.J. Goossens, J. Solid State Chem. 174 (2003) 198.

[4] S.Y. Isotomin, J. Grins, G. Svensson, O.A. Drozhzin, V.L. Kozhevnikov, E.V. Antipov, J.P. Attfield, Chem. Mater. 15 (2003) 4012.
[5] F. Lindberg, O.A. Drozhzhin, S.Y. Istomin, G. Svensson, F.B. Kaynak, P. Svedlindh, P. Warnicke, A. Wannberg, A. Mellergard, E.V. Antipov, J. Solid State Chem. 179 (2006) 1434.
[6] Y. Bréard, A. Maignan, L. Lechevallier, M.-E. Boulon, J.M. Breton, Solid State Sci. 8 (2006) 619.
[7] J.-F. Huang, X. Ni, J.-C. Bao, J.-H. Wu, Chin. J. Struct. Chem. 13 (1994) 350.
[8] J. Li, Y. Duan, H. He, D. Song, J. Alloys Compd 315 (2001) 259.
[9] S.P. Tolochko, I.F. Kononyuk, L.S. Ivashkevich, A. Lyakhov, Inorg. Mater. 29 (1993) 1375.
[10] C.S. Knee, F. Lindberg, N. Khan, G. Svensson, P. Svedlindh, H. Rundlöf, S.G. Eriksson, L. Börjesson, Chem. Mater. 18 (2006) 1354.
[11] Z.P. Shao, S.M. Haile, Nature 431 (2004) 170.
[12] S. Li, Z. Lü, X. Huang, B. Wei, W. Su, Solid State Ionics 178 (2007) 417.
[13] A.C. Larson, R.B. von Dreele, General structure analysis system, Los Alamos National Laboratory Report LA-UR-86-748, 2000.
[14] M. James, D. Cassidy, K.F. Wilson, K.J. Horvat, R.L. Withers, Solid State Sci. 6 (2004) 655.
[15] S.Y. Istomin, O.A. Drozhzhin, G. Svensson, E.V. Antipov, Solid State Sci. 6 (2004) 539.
[16] J.P. Hodges, S. Short, J.D. Jorgensen, X. Xiong, B. Dabrowski, S.M. Mini, C.W. Kimball, J. Solid State Chem. 151 (2000) 190.
[17] P. Nordblad, P. Svedlindh, Experiments on spin glasses, in: P.A. Young (Ed.), Spin Glasses and Random Fields, World Scientific, Singapore, 1997, pp. 123–125.
[18] F. Lindberg, C.S. Knee, G. Svensson, unpublished results.
[19] J.B. Goodenough, Phys. Rev. 100 (1955) 564.
[20] J. Kanamori, J. Phys. Chem. Solids 10 (1959) 87.